Redox-Sensitive Poly(lactic-*co*-glycolic acid) Nanoparticles of Palbociclib: Development, Ultrasound/Photoacoustic Imaging, and Smart Breast Cancer Therapy

Piyush Dhamija,[⊥] Abhishesh Kumar Mehata,[⊥] Rupen Tamang, Jyoti Bonlawar, Vaishali, Ankit Kumar Malik, Aseem Setia, Shailendra Kumar, Ranadheer Reddy Challa, Biplob Koch,* and Madaswamy S. Muthu*

Cite This: https://doi.org/10.1021/acs.molpharmaceut.3c01086

Read Online

ACCESS | Metrics & More | Article Recommendations | SI Supporting Information

ABSTRACT: Breast cancer is one of the leading causes of mortality in women globally. The efficacy of breast cancer treatments, notably chemotherapy, is hampered by inadequate localized delivery of anticancer agents to the tumor site, resulting in compromised efficacy and increased systemic toxicity. In this study, we have developed redox-sensitive poly(lactic-*co*-glycolic acid) (PLGA) nanoparticles for the smart delivery of palbociclib (PLB) to breast cancer. The particle size of formulated PLB@PLGA-NPs (nonredox-sensitive) and RS-PLB@PLGA-NPs (redox-sensitive) NPs were 187.1 ± 1.8 nm and 193.7 ± 1.5 nm, respectively. The zeta potentials of nonredox-sensitive and redox-sensitive NPs were +24.99 ± 2.67 mV and +9.095 ± 1.87 mV, respectively. The developed NPs were characterized for morphological and various physicochemical parameters such as SEM, TEM, XRD, DSC, TGA, XPS, etc. The % entrapment efficiency of PLB@PLGA-NPs and RS-PLB@PLGA-NPs was found to be 85.48 ± 1.29% and 87.72 ± 1.55%, respectively. RS-PLB@PLGA-NPs displayed a rapid drug release at acidic pH and a higher GSH concentration compared to PLB@PLGA-NPs. The cytotoxicity assay in MCF-7 cells suggested that PLB@PLGA-NPs and RS-PLB@PLGA-NPs were 5.24-fold and 14.53-fold higher cytotoxic compared to the free PLB, respectively. Further, the cellular uptake study demonstrated that redox-sensitive NPs had significantly higher cellular uptake compared to nonredox-sensitive NPs and free Coumarin 6 dye. Additionally, AO/EtBr assay and reactive oxygen species analysis confirmed the superior activity of RS-PLB@PLGA-NPs over PLB@PLGA-NPs and free PLB. In vivo anticancer activity in dimethyl-benz(a)anthracene-induced breast cancer rats depicted that RS-PLB@PLGA-NPs was highly effective in reducing the tumor size, hypoxic tumor, and tumor vascularity compared to PLB@PLGA-NPs and free PLB. Further, hemocompatibility study reveals that the developed NPs were nonhemolytic to human blood. Moreover, an in vivo histopathology study confirmed that both nanoparticles were safe and nontoxic to the vital organs.

KEYWORDS: breast cancer, palbociclib, smart delivery, in vivo imaging
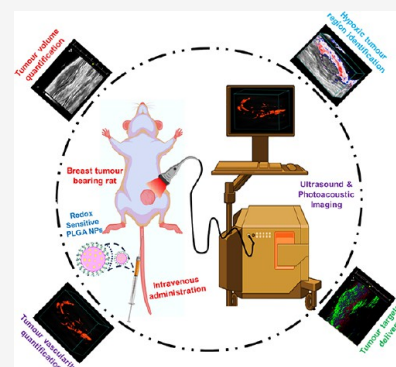
1. INTRODUCTION

Breast cancer is the most common form of malignancy in women.[1] In 2020, breast cancer surpassed lung cancer as the most frequently diagnosed malignancy in women, with approximately 2.3 million new cases, accounting for 11.7% of all cancer diagnoses.[2] Epidemiological studies revealed that by 2030, the global incidence of breast cancer is projected to reach nearly 2 million.[3] Breast cancer mortality rates in developing countries are also higher due to a lack of easy access to diagnosis and treatment facilities and speedy cancer progression and metastasis. The molecular features of hormonal breast tumors include activations of the human epidermal growth factor receptor 2 (HER2) and hormonal receptors (estrogenic and progesterone receptors).[4] Triple-negative breast cancer is a distinct type that does not involve the hormonal receptors

(estrogenic and progesterone receptors) and HER2 typically associated with other forms of breast cancer.[5]

Common approaches to treating breast cancer include surgery, radiation, and systemic therapy.[4] Mastectomy (complete breast removal) or lumpectomy (breast tumor removal) may be necessary depending on the types and stage of the breast cancer. Different types of systemic therapies have been utilized to treat breast cancer, such as chemotherapy, immunotherapy, poly(ADP-ribose) polymerase suppression in mutated BRCA

tumors, HER2-directed treatment for HER2-positive disease, endocrine treatment for hormone receptor-positive breast cancer, and bone stabilizing agents.[4] Chemotherapy is the use of anticancer medications to treat malignant cells. Before surgery, chemotherapy can be used to reduce the tumor's size and, in some cases, make breast-conserving surgery possible instead of a mastectomy. Hormone therapy targets hormone-sensitive breast cancer by inhibiting the interaction of hormones to receptors on cancer cells or reducing the body's hormonal synthesis.[6]

Poly(lactic-*co*-glycolic acid) (PLGA) is a commonly used polymer for nanoparticles (NPs) synthesis and drug delivery due to its biocompatibility, biodegradability, and ease of surface modification.[7−9] Biotransformation of PLGA involves hydrolysis of the ester bond in PLGA at acidic pH, which results in the degradation of PLGA into lactic acid and glycolic acid that can further enter into glycolysis and Kreb's cycle, thereby avoiding the concern of long-term toxicity.[10] The disadvantage of PLGA-NPs is that they cannot interact specifically with target cells or proteins and, thus, are unable to accumulate in the target tissue. However, PLGA-NPs functionalized with the targeting agent are capable of delivering the loaded drug to the targeted site.[11] PLGA, approved by the FDA and widely utilized as a nanocarrier in clinical applications, offers several benefits. The drug-delivery systems formulated with PLGA are biocompatible, nontoxic, and biodegradable.[8]

Vitamin E-PEG 1000-succinate (TPGS) is an amphiphilic material with many pharmaceutical applications and is recognized as the GRAS element by USFDA.[12,13] It is widely used as a surfactant for developing different varieties of drug-delivery molecules. Additionally, TPGS has the ability to inhibit P-gp efflux pumps that prevent the development of resistance of anticancer agents toward cancer therapy. Moreover, TPGS prevents the efflux of the drug out of cancer cells and thus potentiates anticancer efficacy. It has a polar head and lipophilic tail component with 0.02% CMC and 13.2 HLB value.[14] In addition, chemical alteration of the structure of TPGS by various conjugations may enhance the efficacy of NPs. When TPGS is coadministered with anticancer drugs, their availability at the site of action and their cytotoxicity are improved.[15]

Moreover, the utilization of redox-sensitive nanomedicine exhibits notable effectiveness, selectivity, and sensitivity toward tumors. The concentration of glutathione (GSH), a tripeptide that included cysteine, is significantly higher (>20 mM) in the microenvironment of tumor cells in contrast to its concentration in the bloodstream (2−20 μM). This disparity in GSH levels enables the rapid release of antineoplastic agents from redox-responsive NPs that are constructed with redox-sensitive disulfide (S−S) bonds. The cleavage of the S═S bonds will initiate the release of drugs from nanosystems located in close proximity to cancer cells. Recently, in a study, Viswanadh et al. demonstrated the effectiveness of docetaxel-loaded redox-sensitive NPs toward lung cancer. In vitro anticancer activity in lung cancer cells also supported the superior activity of redox-sensitive NPs over nontargeted NPs.[16] Palbociclib (PLB) is a chemotherapeutic agent used to treat advanced-stage breast cancer. PLB is the cyclin D-CDK4/6 inhibitor that inhibits the phosphorylation of retinoblastoma protein, thereby restricting the cell cycle progression from the G1 to S phase. PLB has low toxicity and is approved by FDA for breast cancer therapy.[17−19]

Therefore, a potential advantage of the PLB-loaded redox-sensitive PLGA-NPs for breast cancer is the therapy proposed here for evaluation. Initially, 4-amino thiophenol (4-ATP) was

covalently linked with TPGS-COOH, named as TPGS-SH.[20] Additionally, the NPs were prepared by using emulsion-solvent evaporation technique, and the drug was entrapped into the nonredox-sensitive and redox-sensitive NPs.[16] It was observed from a previous report that NPs having TPGS-SH on their surface is shown to accumulate in tumors more effectively in vivo. Recently, Setia et al., in a study, demonstrated that redox-sensitive TPGS micelles significantly accumulated in lung cancer cells compared to nonredox-sensitive TPGS micelles, which was supported by optical imaging and ultrasound/photoacoustic imaging.[21]

Polymer disulfide bonds of NPs cleave in elevated GSH concentrations of the tumor microenvironment, resulting in drug release inside the cells.[22] For the first time in the literature, we have presented a novel approach to drug delivery by the incorporation of TPGS-SH, a redox-sensitive polymer, into PLGA-NPs. So far, no research paper has been reported on PLGA/TPGS-SH or PLGA/PLB or any of these combinations. Additionally, the formulation was designed to be entirely new. This developed PLGA-based formulation of PLB has been formulated and evaluated for the first time in breast cancer therapy through ultrasound and photoacoustic imaging. Moreover, another novelty of the developed formulation is that the PLGA-based formulation is stable and scalable for large-scale production. This design capitalizes on the elevated levels of GSH in the tumor microenvironment, triggering the cleavage of disulfide bonds and facilitating the release of the loaded drug, specifically at the tumor site. The developed delivery system was loaded with PLB (therapeutic agent) or indocyanine (ICG, imaging agent) for breast cancer imaging and therapy. Moreover, the developed formulations were characterized for their physicochemical properties, morphology, and in vitro evaluation such as in vitro release, cellular uptake studies, cytotoxicity, apoptosis, and reactive oxygen species generation. Additionally, the in vivo safety study by histopathology, breast tumor targeting efficiency, and anticancer efficacy of prepared formulations were evaluated by ultrasound/photoacoustic imaging.

2. MATERIALS AND METHODS

2.1. Materials. TPGS was provided as a gift sample by Antares Health Products, Inc. as a gift sample. PLB was received as a gift sample from Sun Pharmaceutaicals Industries Ltd. PLGA (50:50) was obtained from Sigma Aldrich, India. A dialysis membrane of 1 KD was obtained from Spectrum Laboratories Inc. Human breast cell line MCF-7 was purchased from NCCS Pune in India. Cell Clone (Genetix Biotech Asia Pvt. Ltd.) provided DMEM, FBS, trypsin-EDTA, penicillin-streptomycin solutions, 12-well cell culture plates, and 6-well plates. 96-well plates and T-25 cell culture flasks were obtained from Eppendorf. Other reagents used were of analytical quality.

2.2. Methods. *2.2.1. Synthesis of TPGS-SH.* TPGS-SH was prepared as per our previously reported method.[16] The synthesis of TPGS-SH involved the utilization of EDC and NHS as starting reagents to facilitate the interaction between the carboxylate groups present on TPGS and the primary amine of 4-ATP through carbodiimide chemistry. EDC and NHS were added in the 2:1 ratio to TPGS-COOH; this mixture was gently agitated for 3 h at 25 °C and pH 5. The 4-ATP ethanolic solution was then added in a 1:1 molar ratio of 4-ATP and TPGS-COOH and agitated at 4 °C in the dark under a nitrogen atmosphere overnight. The pH was then adjusted to 7 using sodium borohydride. Ethyl alcohol was used to carry out the

precipitation. After that, the purified solution was lyophilized. The thiolated TPGS pale yellow product was then collected.[16] The synthesized TPGS-SH was characterized by Fourier transform infrared (FTIR, Nicolet iS5, Thermo Electron Scientific Instruments LLC) spectroscopy between 4000 and 500 cm^{-1}.[23,24] Schematic representation of TPGS-SH synthesis and assembly of the disulfide bond of TPGS-SH has been presented in Figure 1A,B.
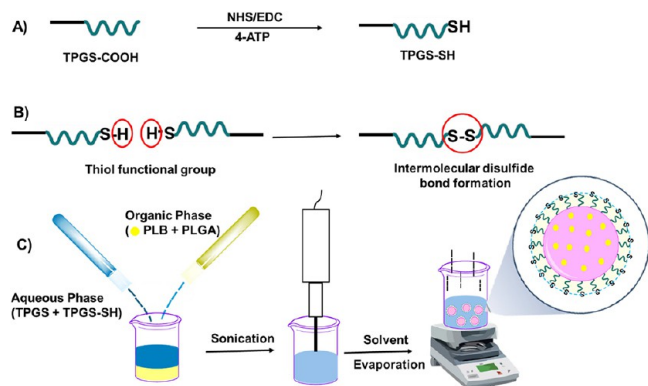
Figure 1. Schematic representation of (A) synthesis of TPGS-SH, (B) assembly of disulfide intermolecular bond, and (C) preparation of redox-sensitive NPs.

2.2.2. Synthesis of PLGA-NPs. The emulsion-solvent evaporation technique was utilized to fabricate PLB-entrapped PLGA-NPs. Briefly, PLGA (20 mg) and PLB (3 mg) were dissolved in 2 mL of dichloromethane (DCM). The aqueous phase was prepared by dissolving TPGS (10 mg) in 7.5 mL of distilled water (DW). The PLB and PLGA containing organic solvents were then transferred to the continuous phase and probe sonicated for 4 min. DCM was removed from the synthesized PLGA-NPs under magnetic stirring.[25]

Similarly, PLB-entrapped redox-sensitive PLGA-NPs were prepared with a slight modification. Briefly, PLGA (20 mg) and PLB (3 mg) were dissolved in 2 mL of DCM. The aqueous phase was prepared by dissolving TPGS (5 mg) and TPGS-SH (5 mg) in 7.5 mL of DW. The PLB and PLGA containing organic solvents were then transferred to the continuous phase and probe sonicated for 4 min. The organic solvent was removed from the synthesized PLGA-NPs under magnetic stirring.[25]

Further, Coumarin 6 (C6) or ICG- loaded PLGA-NPs were prepared as per the above method by replacement of PLB with 0.3 mg of C6 or ICG. The developed NPs were centrifuged, and the obtained pellets were washed with DW and redispersed in the normal saline. The detailed composition of the developed NPs has been presented in Table 1. Schematic representation of the synthesis of redox-sensitive NPs has been presented in Figure 1C.

2.3. Characterization of NPs. *2.3.1. Elman's Assay.* The Elman's assay capable of estimating the percentage of thiol modification in the samples. Briefly, 0.16 mL of Elman's reagent (1 mg/mL in PBS, pH 8) was mixed with 0.08 mL of synthesized nanoformulation in a 96-well plate. The molar absorption coefficient of Elman's reagent was spectrophotometrically determined at 412 nm, and the percentage of thiol modification was determined by using a standard curve.[26]

2.3.2. Size Distribution and Zeta Potential. The particle size (PS) and polydispersity (PDI) of fabricated PLGA-NPs were assessed by a Malvern Zetasizer Nano ZS90. The Malvern zeta

Table 1. Formula of Nonredox-Sensitive and Redox-Sensitive PLGA-NPs[a]

Batches	PLGA (mg)	TPGS (mg)	TPGS-SH (mg)	PLB (mg)	ICG (mg)	C6 (mg)
PLGA-NPs	20	10				
PLB@PLGA-NPs	20	10		3		
RS-PLB@PLGA-NPs	20	5	5	3		
ICG@PLGA-NPs	20	10			0.3	
RS-ICG@PLGA-NPs	20	5	5		0.3	
C6@PLGA-NPs	20	10				0.3
RS-C6@PLGA-NPs	20	5	5			0.3

[a]PLB@PLGA-NPs: PLB-entrapped PLGA-NPs; RS-PLB@PLGA-NPs: PLB-entrapped redox-sensitive PLGA-NPs; ICG@PLGA-NPs: Indocyanine green-entrapped PLGA-NPs; RS-ICG@PLGA-NPs: Indocyanine green-entrapped redox-sensitive PLGA-NPs; C6@PLGA-NPs: Coumarin 6-entrapped PLGA-NPs; RS-C6@PLGA-NPs: Coumarin 6-entrapped redox-sensitive PLGA-NPs.

sizer Nano ZS was utilized to determine the zeta potential (ZP) values of NPs. The formulations were examined for surface charge assessments after the proper sample dilution.[27]

2.3.3. Scanning Electron Microscopy. PLB@PLGA-NPs and RS-PLB@PLGA-NPs were morphologically examined through a Nova Nano SEM 450 microscope. Ten times diluted samples with Millipore ultrapure water were used, and a single drop of the diluted sample was placed on the coverslips, followed by overnight drying at 40 °C. The carbon-coated slides were subjected to the scanning electron microscopy (SEM) analysis. Images were taken at a 15 kV voltage and 100−250 KX magnification.[28]

2.3.4. Transmission Electron Microscopy. Transmission electron microscopy (TEM, Philips CM-12. Fullerton, CA) was utilized to determine the morphologies of PLB@PLGA-NPs and RS-PLB@PLGA-NPs. The NPs underwent sonication for 2 min after being diluted 10 times with purified water. On the carbon-coated TEM grids, a drop was placed and dried overnight before examination.[29]

2.3.5. Surface Chemistry. The surface chemistry of PLB@PLGA-NPs and PLB@PLGA-NPs was examined by X-ray photoelectron spectroscopy (XPS) (K- Alpha, Thermo Fischer Scientific, USA) at the binding energy between 50 to 800 eV. The concentrated NPs sample was applied on a coverslip and subjected to overnight drying and scanned for the elemental composition by XPS.[30]

2.3.6. Differential Scanning Calorimetry. DSC-60 Plus (Asia Pacific Pvt. Ltd.) calorimeter was employed to assess the interactions of excipients (TPGS, TPGS-COOH, TPGS-SH, and PLGA) with the drug (PLB) at temperatures ranging from 25 to 400 °C with 10 °C/min heating rate. The heating process was carried out in a standard aluminum pan. An empty, loosely covered aluminum pan was used as the reference.[31]

2.3.7. Thermogravimetric Analysis. TGA-50 (M/s Shimadzu Asia Pacific Pvt Ltd., Japan) analyzer was utilized to detect the thermal stability of PLB in PLGA-NPs. The NPs were subjected to 10 °C/min heating rate and 50 mL/min nitrogen flow rate with heating ranging from 25 to 600 °C.[32]

2.3.8. X-ray Diffraction. The crystalline nature and purity of the compounds was examined by X-ray diffraction (XRD). The

XRD spectra of TPGS, TPGS-SH, PLGA, PLB, PLB@PLGA-NPs, and RS-PLB@PLGA-NPs were obtained by XRD (Rigaku, Japan). The diffractograms were collected at 2 theta angles ranging between 20° and 50°, and 40Kv tube voltage was used to set 10° min/scan speed.[33]

2.3.9. Entrapment Efficiency. The entrapment efficiency (EE) of the developed NPs was determined by an indirect method. Ultraviolet−visible (UV−vis) spectroscopy was utilized to determine the EE of PLB in the synthesized nanoformulation. The separation of the NPs involved centrifuging 1 mL of the formulation at 14,000 rpm for 90 min using a Remi cooling centrifuge (CM-12 Plus Mumbai, India) at 4 °C. The supernatant of the centrifuged sample was collected and absorbance was measured using UV−vis spectroscopy at 365 nm, and PLB was quantified by comparing with the standard calibration curve.[34] The following formula was used for the calculation of the EE of PLB in the developed NPs.

$$\% \text{ Entrapment} = \frac{\text{Total amount of PLB used} - \text{Amount of PLB unentrapped}}{\text{Total amount of PLB used}} \times 100 \quad (1)$$

2.3.10. Assessment of Storage Stability and Serum Stability. Lyophilized powders of PLB@PLGA-NPs and RS-PLB@PLGA-NPs were evaluated for changes in PS, PDI, and EE following storage at room and freezing temperatures. Briefly, 10 mL vials containing lyophilized powder of PLB@PLGA-NPs and RS-PLB@PLGA-NPs were stored at 2−8 and 25 °C. Samples were withdrawn after 2 months, and their physicochemical parameters were assessed to compare the storage stability of the nanoformulation with its day 1 data.[35]

The in vitro physiological stability of the produced NPs was evaluated by using female rat serum. In brief, equal amounts of serum and NPs suspension were incubated for 24 h at 37 °C. Following incubation, the NPs were collected and assessed for entrapment effectiveness, ZP, and PS.

2.4. In Vitro Study. *2.4.1. PLB Release Profile.* The dialysis bag diffusion method was utilized to investigate the drug release from PLB@PLGA-NPs and RS-PLB@PLGA-NPs at pH 5.5 and pH 7.4 with or without 5 and 20 μM of GSH. A dialysis bag of 1 KD was filled with 2 mL of the NP formulation, and then the dialysis bag was placed at 7.4 pH PBS (50 mL) and 5.4 pH acetate buffer, and the entire setup was mildly stirred at 150 rpm and maintained at 37 ± 0.5 °C. At different time points, 3 mL of sample was taken and replaced with the same volume of fresh media. An UV−visible spectrophotometer was employed to quantify the amount of PLB in the collected samples at 365 nm λ_{max}.[36] Similarly, an equivalent amount of PLB was dissolved in acidified polyethylene glycol, and in vitro release was performed at both pH.

2.4.2. In Vitro Hemocompatibility Study. 2.4.2.1. Blood Smear. Human blood (10 mL) was collected from the blood bank. Then, 200 μL of phosphate-buffered saline (PBS) as a -ve control, 200 μL of DW as a -ve control, 200 μL of 0.3 mg/mL PLB as the model (drug) control, 200 μL of PLB@PLGA-NPs, and 100 μL of RS-PLB@PLGA-NPs were incubated at 4 °C for 24 h with 0.8 mL of blood. A single drop of the prepared blood sample was then processed as a film and stained with Leishman solution to observe the cellular behavior of the blood. The excess stain was removed by washingwith 7.4 pH PBS. Bright-field microscopy at 40× magnification was employed to visualize the morphological changes in the blood cell.[37]

2.4.2.2. Hemolytic Assay. Hemolytic assay was used to evaluate the safety of PLB, PLB@PLGA-NPs, and RS-PLB@PLGA-NPs in human blood. The nanoformulation was first centrifuged at 12,000 rpm, and then the supernatant was removed. The pellet so formed was then washed and mixed with saline, and then finally 0.2 mL of NPs were incubated with 0.8 mL of RBCs of human blood for 24 h. The samples were centrifuged at 2000 rpm, and the collected supernatant was analyzed by a microplate reader at 545 nm.[38] The % hemolysis was calculated using the following formula:

$$\% \text{ Haemolysis} = \frac{\text{Abs } T - \text{Abs } C}{\text{Abs } 100\% - \text{Abs } C} \times 100 \quad (2)$$

2.4.3. Cytotoxicity Analysis. The cytotoxicity of RS-PLB@PLGA-NPs, PLB@PLGA-NPs, and PLB was evaluated by using the standard MTT test on the breast cancer cell line MCF-7. MCF-7 cell lines were seeded into 96-well plates at a density of 1 × 10^4 cells per well with DMEM, and the cells were then incubated overnight for cell attachment. After removing the medium, the cells were treated with varying concentrations of RS-PLB@PLGA-NPs, PLB@PLGA-NPs, and PLB and then incubated for 24 h. Following that, 100 μL of MTT solution (5 mg/mL in PBS) was added to each well after discarding the spent media. The experimental plate was then incubated at 37 °C for 2 h, and then the generated formazan crystals were dissolved by adding 100 μL of DMSO to the well plates.[39] The percent cell viability may be determined by

$$\% \text{Cell Viability} = \frac{\text{Absorbance of treated cells}}{\text{Absorbance of control cell}} \times 100 \quad (3)$$

2.4.4. Cellular Uptake Study. Coumarin 6 (C6) is a fluorescent dye widely used for the evaluation of the cellular uptake study. The cellular uptake of C6@PLGA-NPs, RS-C6@PLGA-NPs, and free C6 was done by confocal microscopy (super-resolution confocal microscopy, Leica, Germany). In each well of a 6-well plate, 1× 10^5 MCF-7 cells were seeded on a coverslip and left to grow for 24 h. The cells were then treated with C6@PLGA-NPs, RS-C6@PLGA-NPs, and free C6 for 5 h. After that, 1 mL of PBS was used to wash the cells. Paraformaldehyde fixation was performed thereafter, and 15 min of propidium iodide staining was followed to stain the cellular nucleus. Cells were then observed using a confocal microscope.[40]

2.4.5. Acridine Orange/EtBr Assay. Based on the integrity of the cell membrane, one can distinguish between the dead and live cells using the acridine orange (AO) and ethidium bromide (EtBr) dual staining method. This test can tell healthy cells apart from necrotic, early, and late apoptotic cells. In a 12-well culture plate, MCF-7 cells were seeded at a density of 5 × 10^4 cells per well and allowed to adhere overnight. An equivalent concentration of PLB and PLB-loaded NPs was used to treat MCF-7 cells. The cells were then incubated for 24 h. Finally, after labeling the cells with AO/EtBr, images were taken in the green and red channels using an inverted fluorescent microscope (EVOS live cell imaging equipment from Life Technologies).[41,42]

2.4.6. Reactive Oxygen Species Analysis. The level of intracellular reactive oxygen species (ROS) generation for both free PLB and the prepared formulation was investigated using the oxidation-sensitive fluorescent probe 2′, 7′ -dichlorodihydrofluorescein diacetate (DCFH-DA). Briefly, 5 × 10^4 MCF-7 cells were seeded in a 12-well plate and incubated overnight for the cell's attachment to the flask. The cells were subsequently

Table 2. PS, PDI, ZP, and EE of Developed NPs[a]

Batches	PS (nm) (mean ± SD*)	PDI (mean ± SD*)	ZP (mV) (mean ± SD*)	EE (%) (mean ± SD*)	IC_{50} (μg/mL)
PLB					45.90 ± 2.11
PLGA-NPs	186.8 ± 1.5	0.124 ± 0.03	20.34 ± 1.37		
PLB@PLGA-NPs	187.1 ± 1.8	0.132 ± 0.01	24.99 ± 2.67	85.48 ± 1.29	8.75 ± 0.86
RS-PLB@PLGA-NPs	193.7 ± 1.5	0.143 ± 0.02	9.95 ± 1.87	87.72 ± 1.55	3.15 ± 0.24
ICG@PLGA-NPs	190.4 ± 1.9	0.137 ± 0.03	26.44 ± 2.34	87.37 ± 2.32	
RS-ICG@PLGA-NPs	197.6 ± 1.2	0.149 ± 0.05	17.90 ± 1.45	88.98 ± 2.65	
C6@PLGA-NPs	188.7 ± 1.6	0.170 ± 0.08	24.39 ± 1.98	87.89 ± 1.79	
RS-C6@PLGA-NPs	196.7 ± 1.2	0.105 ± 0.02	16.78 ± 1.76	90.29 ± 1.34	

[a]PLB@PLGA-NPs: PLB-entrapped PLGA-NPs; RS-PLB@PLGA-NPs: PLB-entrapped redox-sensitive PLGA-NPs; ICG@PLGA-NPs: Indocyanine green-entrapped PLGA-NPs; RS-ICG@PLGA-NPs: Indocyanine green-entrapped redox-sensitive PLGA-NPs; C6@PLGA-NPs: Coumarin 6-entrapped PLGA-NPs; RS-C6@PLGA-NPs: Coumarin 6-entrapped redox-sensitive PLGA-NPs.

exposed to RS-PLB@PLGA-NPs, PLB@PLGA-NPs, and free PLB for 24 h. After being washed with PBS, the cells were treated with 10 mM DCFH-DA for 30 min at 37 °C. The qualitative assessment of the ROS was performed by capturing the images of the cells using fluorescence microscopy.[43]

2.5. In Vivo Study. *2.5.1. Histopathology Study.* Animals used in this study were approved by the Institutional Animal Ethics Committee (IAEC), IIT (BHU) Varanasi (IAEC approval number IIT(BHU)/IAEC/2023/088). The in vivo studies were conducted at the IIT (BHU), Varanasi in accordance with the standards specified by the IAEC. Each animal experiment followed strict guidelines published by the National Research Council.

Saline, PLB, PLB@PLGA-NPs, and RS-PLB@PLGA-NPs were administered at 5.91 mg/kg dose to different rat groups three times at 3-day intervals. On the 15th day, animals were euthanized, and then the vital organs like the heart, liver, lungs, and kidneys were extracted and preserved in 10% V/V formalin. The paraffin box was used to place the specimen and sliced at 5 μm thickness. Hematoxylin and eosin (H & E) were utilized to stain the slices, and then histopathologic changes were observed under the microscope.[44]

2.5.2. In Vivo Antitumor Activity by Photoacoustic and Ultrasound Imaging. Mammary cancer was induced in Sprague−Dawley rats, aged 120 days, by administration of sesame oil-diluted DMBA in the breast pad at the dose of 50 mg/kg of body weight. The formation of breast tumor was confirmed by ultrasound imaging. Afterward, rats were divided into four groups, each with three animals. Groups 1 and 2 received saline and PLB, respectively. PLB@PLGA-NPs and RS-PLB@PLGA-NPs were administered to groups 3 and 4 at 5.91 mg/kg doses of PLB at 3-day intervals. Ultrasound and photoacoustic imaging were used to visualize the changes in the tumor volume, hypoxia level, and tumor vascularity at regular time intervals. Briefly, 1.5% isoflurane was used to anesthetize the rats. Further, an ultrasonic gel (Supragel, LCH, France) was placed between the transducer and the skin. The imaging of tumors was performed using ultrasound and photoacoustic imaging system (Visual Sonics Vevo 3100 System, FUJIFILM, Canada). 3D scan of ultrasound images were digitally captured. VevoLAB 1.7.2 software was used to manually delineate tumor margins in coronal planes. Next, a volume was calculated for each coronal slice using the software. Photoacoustic imaging with OxyHemo-Mode was utilized to assess the hypoxic volumes, and power Doppler was used for accessing the tumor vascularity.[45,46]

2.5.3. In Vivo Tumor Targeting Study. Sprague−Dawley rats with DMBA-induced breast cancer weighing 150−200 g were employed for the experimentation. ICG is a photoacoustic

sensitive dye widely used for photoacoustic-based in vivo imaging. Group 1, group 2, and group 3 receive ICG, ICG@PLGA-NPs, and RS-ICG@PLGA-NPs, respectively, at 12 μg/kg dose. Rats were anesthetized using 1.5% isoflurane. A thin layer of ultrasonic gel was then placed between the transducer and the skin (Supragel, LCH, France). A Vivo 3100 System (Fujifilm VisualSonics Inc., Canada) was employed for the imaging of tumors. An optical wavelength of 664 nm was used for photoacoustics excitation. 3D scans of ultrasound images were digitally captured. VevoLAB 1.7.2 software was employed for processing of data. After 30 min of injection of ICG control and ICG-loaded NPs, the PA signal was captured.[47]

2.6. Statistical Analysis. Results were calculated as mean (n = 3) ± standard deviation. One-way ANOVA was used for the statistical analysis. Differences are statistically significant at a ns ($p > 0.05$), * ($p < 0.05$), ** ($p < 0.01$), and *** ($p < 0.001$).

3. RESULTS AND DISCUSSION

3.1. FTIR Spectroscopy. The IR spectra of TPGS, TPGS-COOH, and TPGS-SH were compared by using FTIR analysis (Figure S1). The IR spectrum of TPGS and the IR spectrum of TPGS-COOH demonstrated broad OH peaks at 3467.7 and 3465.9 cm^{-1}, respectively. Moreover, N−H bending and N−H stretching were detected in TPGS-SH spectra at 1552.6 and 3419.2 cm^{-1}, respectively. Carbonyl groups TPGS, TPGS-COOH, and TPGS-SH exhibited IR peaks at 1746.5, 1734.6, and 1660.5 cm^{-1}, respectively. C−O was also detected in the IR spectra of TPGS, TPGS-COOH, and TPGS-SH at 1244.4, 1131.5, and 1214.2 cm^{-1}, respectively.[48] All observed FTIR peaks from samples are presented in Table S1.

3.2. Elman's Assay. The degree of TPGS-SH modification was spectrophotometrically determined by Elman's assay. The RS-PLB@PLGA-NPs (0.5 mg/mL; TPGS-SH) were mixed with Elman's reagent, and the amount of thiol modification was analyzed by a spectrophotometer at 402 nm. The percentage of TPGS-SH conjugated with RS-PLB@PLGA-NPs was found to be 78.45 ± 2.54%.

3.3. Size Distribution and ZP. The PS of the nano-formulation of PLB@PLGA-NPs, RS-PLB@PLGA-NPs, ICG@PLGA-NPs, RS-ICG@PLGA-NPs, C6@PLGA-NPs, and RS-C6@PLGA-NPs was 187.1 ± 1.8, 193.7 ± 1.5, 190.4 ± 1.9, 197.6 ± 1.2, 188.7 ± 1.6, and 196.7 ± 1.2 nm (Table 2). The ZP of the NP formulation of PLB@PLGA-NPs, RS-PLB@PLGA-NPs, ICG@PLGA-NPs, and RS-ICG@PLGA-NPs was found to be +24.99 ± 2.67 mV, + 9.095 ± 1.87 mV, + 26.44 ± 2.34 mV and +17.90 ± 1.45 mV (Table 2). Based on the PS data, it was noted that all NPs fall within the favorable range of 200 nm. This size range is particularly advantageous for leveraging the

enhanced permeation and retention (EPR) effect in cancer delivery, primarily owing to the leaky nature of tumor vasculature.

Moreover, considering the significance of the ZP in NP-based drug delivery to cancer, it is worth noting its crucial role. ZP, which characterizes the surface charge of NPs, influences their stability, dispersibility, and interaction with biological systems. In cancer drug delivery, NPs with appropriate ZPs can facilitate efficient targeting, cellular uptake, and intracellular drug release, thereby enhancing therapeutic efficacy while minimizing off-target effects. The ZP of the NPs was in the range of 9−27 mV, which is optimum for the stability of the NPs. Further, PDI values of all developed NPs were below 0.2, which indicates their uniform size distribution.
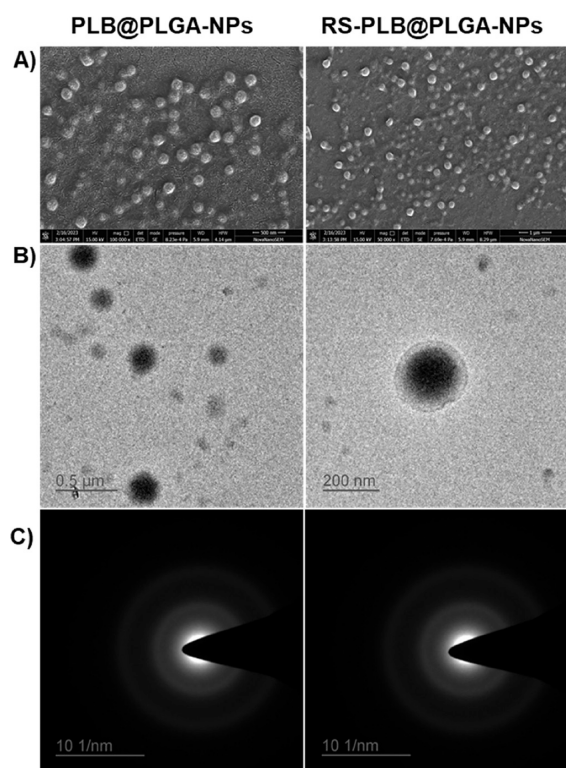
3.4. EE. The EE of PLB in PLB@PLGA-NPs and RS-PLB@PLGA-NPs was 85.48 ± 1.29% and 87.72 ± 1.55%. The percent entrapment of ICG in ICG@PLGA-NPs and RS-ICG@PLGA-NPs was 87.37 ± 2.32% and 88.98 ± 2.65%. The percent entrapment of C6 in C6@PLGA-NPs and RS-C6@PLGA-NPs was 87.89 ± 1.79% and 90.29 ± 1.34% (Table 2). The EE data demonstrated that NPs had better drug-loading capacity for efficient delivery to tumor cells.

3.5. SEM. SEM was employed to examine the size and morphology of the PLB@PLGA-NPs and RS-PLB@PLGA-NPs. Figure 2A displays that the size of the fabricated

Figure 2. (A) SEM, (B) TEM, and (C) SAD images of PLB@PLGA-NPs and RS-PLB@PLGA-NPs.

nanoformulation was less than 200 nm. The NPs exhibit smooth surface and circular shape and are monodispersed and crack-free. The NPs with size below 200 nm have added advantages of EPR effect to cancer cells.

3.6. TEM. The size, shape, and external morphology of PLB@PLGA-NPs and RS-PLB@PLGA-NPs were revealed by TEM. The TEM images demonstrated that the NPs have a spherical

shape and a smooth surface. The selected area diffraction (SAD) images of the PLB@PLGA-NPs and RS-PLB@PLGA-NPs showed diffuse rings, indicating their amorphous behavior (Figure 2B,C).

3.7. Differential Scanning Calorimetry. Differential Scanning Calorimetry (DSC) was employed to assess the thermal behavior of polymeric NPs. Figure S2A depicts the thermograms of TPGS, TPGS-COOH, TPGS-SH, PLGA, PLB@PLGA-NPs, and RS-PLB@PLGA-NPs. The endothermic peak for TPGS, TPGS-COOH, and TPGS-SH was detected at 36.87, 126.28, and 124.57 °C, respectively. PLGA displays an endothermic peak at 48.78 °C. However, PLB displays a sharp endothermic peak at 272.83 °C. Moreover, the endothermic peak of PLB was not detected in PLB@PLGA-NPs and RS-PLB@PLGA-NPs, indicating successful entrapment of the drug within the NPs, highlighting their potential for controlled drug release and enhanced stability. These findings suggest promising applications in redox-sensitive-based drug delivery, emphasizing the feasibility of utilizing PLGA-based NPs as effective carriers for therapeutic agents, with implications for improving therapeutic efficacy while minimizing adverse effects.
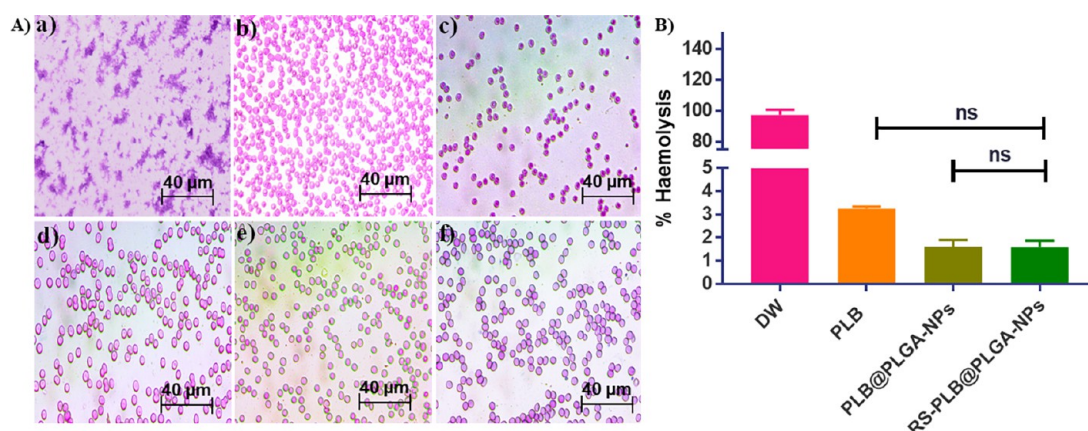
3.8. Thermogravimetric Analysis. Thermogravimetric analysis (TGA) is useful for understanding the thermal stability of nanomaterials and polymer composites when heated at a predetermined rate and temperature. TPGS, TPGS-COOH, TPGS-SH, PLGA, PLB, PLB@PLGA-NPs, and RS-PLB@PLGA-NPs loses 98.39, 98.34, 98.33, 71.82, 99.25, 57.7, 81.24, 96.44, and 97.47% of its initial weight between 25 and 600 °C (Figure S2B). PLB@PLGA-NPs displays an initial weight loss of 0.75% at 48.24 °C due to loss of water. Afterward, a continual weight loss of 43.82% was observed between 223.44 and 311.12 °C due to decomposition of polymers. Thereafter, a progressive weight loss of 31.17% was observed between 312.18 and 403.81 °C due to degradation of the drug. Moreover, a % weight loss of 14.38% was observed between 404.21 and 599.35 °C. RS-PLB@PLGA-NPs show an initial weight loss of 0.77% at 47.84 °C due to water loss. Thereafter, a progressive weight loss of 41.47% was observed between 221.89 and 302.62 °C due to the decomposition of polymers. Then, a gradual weight loss of 33.02% was observed between 303.61 and 395.72 °C due to degradation of the drug. Further, a weight loss of 14.84% was observed between 396.15 and 553.60 °C. Moreover, a weight loss of 0.13% was observed between 554.62 and 596.60 °C. PLB displayed the first weight loss at 294.92 °C. Thereafter, a gradual weight loss of 44.33% was observed between 295 and 436.08 °C. Afterward, 13.59% weight loss was observed between 437 and 599.73 °C. PLGA shows the first weight loss at 176.25 °C. Thereafter, a progressive a weight loss of 95.92% was observed between 226.54 and 387.65 °C. TPGS displayed an initial weight loss at 55.87 °C. Further, a gradual weight loss of 93.71% was observed between 271.79 and 419.08 °C. TPGS-COOH showed an initial weight loss at 42.43 °C. Thereafter, a progressive weight loss of 78.98 °C was observed between 219.87 and 419.86 °C. TPGS-SH exhibited the first weight loss at 37.73 °C. Afterward, TPGS-SH lost 14.9% weight between 111.58 and 223.66 °C followed by a continual weight loss of 66.32% between 224.34 and 417.42 °C. The physical mixture loses its first weight at 47.40 °C. Then, 16.27% weight was lost gradually from 206.04 to 264.95 °C. Afterward, 44.12% weight loss was observed between 265.98 and 392.64 °C. TPGS, TPGS-COOH, TPGS-SH, PLGA, PLB, physical mixture, PLB@PLGA-NPs, and RS-PLB@PLGA-NPs lose 50% of their initial

Figure 3. (A) Blood smear images of (a) DW, (b) pure blood, (c) saline, (d) PLB, (e) PLB@PLGA-NPs, and (f) RS-PLB@PLGA-NPs. (B) Percentage hemolysis of DW, PLB, PLB@PLGA-NPs, and RS-PLB@PLGA-NPs.

weight at 385.95, 380.61, 345.84, 283.88, 346.8, 460.28, 311.99, 311.11, and 306.10 °C, respectively.

TGA provides comprehensive insights into the thermal stability and decomposition behavior of the various nanomaterials and polymer composites investigated in this study. The results indicate significant differences in the thermal stability profiles among the tested materials. PLGA, TPGS, TPGS-COOH, and TPGS-SH exhibit relatively high thermal stability with substantial weight loss occurring only at elevated temperatures. PLB, on the other hand, displays relatively lower thermal stability, with significant weight loss observed over a broader temperature range. Entrapment of PLB within PLGA-based NPs (PLB@PLGA-NPs and RS-PLB@PLGA-NPs) enhances their thermal stability to some extent, as evidenced by the delayed onset of decomposition compared to pure PLB. Overall, the TGA findings contribute valuable insights into the thermal characteristics of the various materials and the developed NPs.

3.9. Storage Stability and Serum Stability. The lyophilized powder of PLB@PLGA-NPs and RS-PLB@PLGA-NPs was stored at room temperature as well as freezing temperature and evaluated for the changes in the size, PDI, and EE. The NPs were found to be stable at different temperatures, as revealed by storage stability studies. The EE of PLB@PLGA-NPs and RS-PLB@PLGA-NPs before storage was 84.32 ± 1.37%, and 85.74 ± 2.41%, respectively. The EE of PLB@PLGA-NPs and RS-PLB@PLGA-NPs after storage at 2−8 °C for 60 days was found to be 82.63 ± 1.51% and 83.02 ± 1.63%, respectively. Figure S2C,D demonstrates no significant changes in PS and PDI (Figure S2E,F) of fresh nanoformulation and stored nanoformulation, indicating that the NPs were stable for an extended period.

The serum stability of the prepared NPs was evaluated with respect to PS, PDI, and EE data obtained before and after serum incubation (Figure S3). There were no significant differences observed in the variations of PS, PDI, and EE before and after incubation ($p > 0.05$).

3.10. Surface Chemistry. XPS was used to analyze the elements present over the surface of PLB@PLGA-NPs and RS-PLB@PLGA-NPs (Figure S4A,B). The peaks detected at binding energies of 538.08, 408.58, and 292.08 eV were assigned to O 1s, N 1s, and C 1s. The N 1s, O 1s, and C 1s percent in PLB@PLGA-NPs was 2.56, 28.73, and 68.71%, respectively, whereas for RS-PLB@PLGA-NPs, these were 3.03, 23.75, and 73.22%, respectively. An increase in the N 1s and C 1s signals

was observed, which was due to the attachment of 4-ATP on the RS-PLB@PLGA-NPs. Additionally, a decrease in the number of O 1s was observed, which was attributed to the release of the water molecules during the formation of the amide bond between free carboxylic acid of TPGS and free amine group of 4-ATP. Moreover, the characteristic S 2p peak was observed in RS-PLB@PLGA-NPs, indicating that sulfur is present on the surface of redox-sensitive NPs.

3.11. XRD. The crystalline or amorphous behavior of the NPs was demonstrated by XRD. The sharp peaks were detected in the XRD spectrum of PLB at 2 theta values of 10.249 and 22.39, indicating its crystalline nature. TPGS also shows sharp peaks at 2 theta values of 19.17 and 23.31. However, a sharp peak in TPGS-COOH was observed at a 2 theta value of 15.17. TPGS-SH, PLGA, PLB@PLGA-NPs, and RS-PLB@PLGA-NPs display amorphous characteristics (Figure S4C). The amorphous materials have better solubility and improved bioavailability.

3.12. In Vitro Drug Release Profile. The drug release profile was evaluated at pH 7.4 (Figure S4D) and 5.5 (Figure S4E) with different GSH concentrations. The drug release profile of PLB@PLGA-NPs and RS-PLB@PLGA-NPs showed 39.02 and 28.33% release of drug in the initial 2 h and 72.05 and 68.95% by the end of 24 h at pH 7.4. However, PLB@PLGA-NPs displayed 42.02 and 50.02% within 2 h and 75.05 and 79.05% within 24 h at 5 mM GSH and 20 mM GSH concentrations, respectively. Additionally, RS-PLB@PLGA-NPs showed 47.02 and 54.02% drug release within 2 h, and it was 80.05 and 88.05% within 24 h at 5 mM GSH and 20 mM GSH concentrations, respectively. The in vitro release of PLB from RS-PLB@PLGA-NPs at 20 mM GSH was significantly higher ($p < 0.001$) than that from PLB@PLGA-NPs at pH 7.4.

However, the drug release profile of PLB@PLGA-NPs and RS-PLB@PLGA-NPs showed 39.35 and 41.27% release of drug in the initial 2 h and 74.80 and 78.16% by the end of 24 h at pH 5.5. In contrast, PLB@PLGA-NPs displayed 47.02 and 55.02% within 2 h, and it was 74.05 and 83.05% within 24 h at 5 mM GSH and 20 mM GSH concentrations, respectively. Additionally, RS-PLB@PLGA-NPs showed 52.02 and 67.02% drug release within 2 h, and it was 78.05 and 94.05% within 24 h at 5 mM GSH and 20 mM GSH concentrations, respectively. The in vitro release of PLB from RS-PLB@PLGA-NPs at 20 mM GSH was significantly higher ($p < 0.001$) than that from PLB@PLGA-NPs at pH 5.5. The drug release profile demonstrates that the drug release was more rapid at pH 5.5 in comparison to pH 7.4.
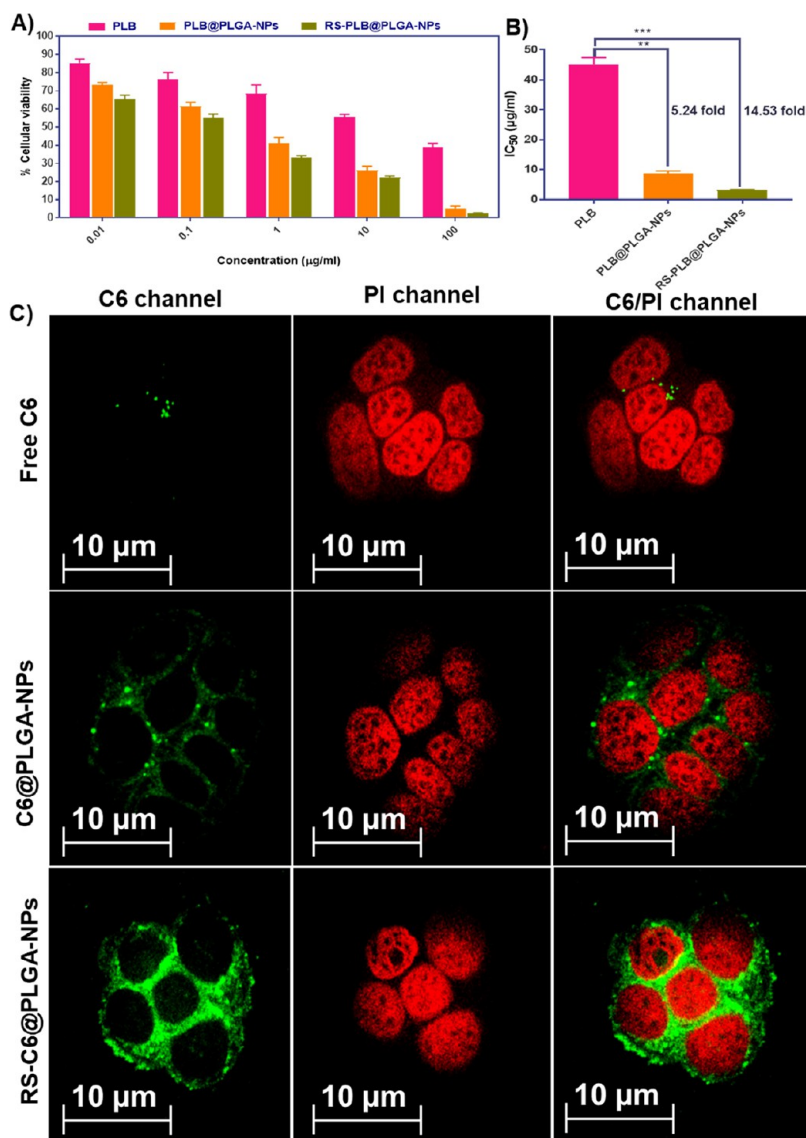
Figure 4. Graphical representation. (A) Cellular viability and (B) IC_{50} value of PLB, PLB@PLGA-NPs, and RS-PLB@PLGA-NPs in MCF-7 cells. (C) CLSM images revealing cellular uptake of free C6, PLB@PLGA-NPs, and RS-PLB@PLGA-NPs in MCF-7 breast cancer cells.

In addition, the release of the drug was enhanced significantly at higher GSH concentrations due to the presence of a disulfide bond in RS-PLB@PLGA-NPs, which are sensitive to GSH.

3.13. Blood Smear. NPs may disrupt the blood coagulation pathway, inflammation, and blood cell lysis. Therefore, the blood safety profile of the saline, the PLB control, PLB@PLGA-NPs, and RS-PLB@PLGA-NPs was compared in a blood smear study. After incubating each sample separately, the blood smear was visualized at a 400× magnification under a bright-field microscope. Blood smear analysis demonstrates that compared to the saline control, the treatment did not show a significant effect on the blood cell morphology. Figure 3A illustrates that PLB, PLB@PLGA-NPs, and RS-PLB@PLGA-NPs did not alter the blood cell morphology.

3.14. Hemolytic Assay. The hemolytic assay was employed to assess the safety of PLB, PLB@PLGA-NPs and RS-PLB@PLGA-NPs in the blood. The percent hemolysis of PLB, PLB@PLGA-NPs and RS-PLB@PLGA-NPs was 3.25 ± 0.08, 1.60 ± 0.30, and $1.59 \pm 0.28\%$ (Figure 3B), respectively, indicating that PLB, PLB@PLGA-NPs, and RS-PLB@PLGA-NPs are non-hemolytic and safe for in vivo administration. As per the ASTM

F756 guidelines, NPs with % hemolysis below 5% are considered safe for the in vivo application. The obtained data demonstrated that all NPs had below 5% of hemolysis.

3.15. Cytotoxicity Analysis. The obtained results showed that the effect of these formulations on cell viability was determined to be in a concentration-dependent manner. The MTT assay performed on MCF-7 demonstrates a substantial decrease in proliferation by RS-PLB@PLGA-NPs, PLB@PLGA-NPs, and PLB. The RS-PLB@PLGA-NPs, PLB@PLGA-NPs, and PLB IC_{50} values were determined to be 3.15 ± 0.24 μg/mL, 8.75 ± 0.86 μg/mL, and 45.90 ± 2.11 μg/mL, respectively. These results showed that these formulations responded to the breast cancer cell line (MCF-7). The findings also imply that formulation RS-PLB@PLGA-NPs is superior to PLB@PLGA-NPs and PLB in terms of efficacy (Figure 4A,B).

The NP-based drug-delivery system evaluated by the cellular viability assay in cancer cells serves as a vital tool for assessing the potential cytotoxic effects of NPs on cancer cells. By evaluating the cellular viability, this assay helps to determine the optimal formulations that are required to kill 50% of the cancer cell populations. Understanding the cytotoxicity profile of NPs aids

in the development of more efficacious anticancer treatments. Hence, from the study, it was observed that PLB@PLGA-NPs and RS-PLB@PLGA-NPs had 5.24- and 14.53-fold cytotoxicity to MCF-7 cells, respectively, compared to free drug.

3.16. Cellular Uptake Study. Studies on the cellular uptake of NPs in cancer cells are crucial for understanding the mechanism of enhancing cancer treatment. Such studies offer insights into the mechanisms underlying NP uptake by cancer cells, thereby elucidating the efficacy of NP-based drug-delivery systems. By understanding the mechanism of NPs internalized into cancer cells, it helps to gain valuable knowledge for the development of more effective strategies for delivering therapeutic agents to cancer cells.

Figure 4C depicts MCF-7 cells after incubation with free C6, C6@PLGA-NPs, and RS-C6@PLGA-NPs. The RS-C6@PLGA-NPs displayed more green fluorescence and higher cytoplasmic green stains compared to the free C6 and C6@PLGA-NPs. In the MCF-7 cell line, our research shows that RS-C6@PLGA-NPs have a higher cellular formulation absorption than C6 alone and C6@PLGA-NPs. Redox-sensitive NPs exhibit increased cellular uptake compared to the control counterparts. This heightened uptake is attributed to the redox-sensitive NPs' greater sensitivity to cancer cells, which typically have elevated levels of GSH.

3.17. AO/EtBr Assay. The cellular morphology and manner of cell death in MCF-7cells induced by RS-PLB@PLGA-NPs, PLB@PLGA-NPs, and PLB following treatment with AO/EtBr dyes were studied using fluorescence microscopy. Control MCF-7 cells (living) have a normal shape as well as green fluorescence in the cytoplasm and nucleus. The MCF-7 cells were treated with RS-PLB@PLGA-NPs, PLB@PLGA-NPs, and PLB at a concentration of 3.15 μg/mL, whereas the control cells (remains untreated). More numbers of cells with nuclear morphological changes, chromatin condensation, and nucleus fragmentation were seen in the RS-PLB@PLGA-NPs-treated cells compared to PLB@PLGA-NPs-treated cells, but such cell alterations were further reduced in PLB-treated cells. Figure 5 depicts the morphological changes in the MCF-7 cells following treatment with the free drug and NP formulations.
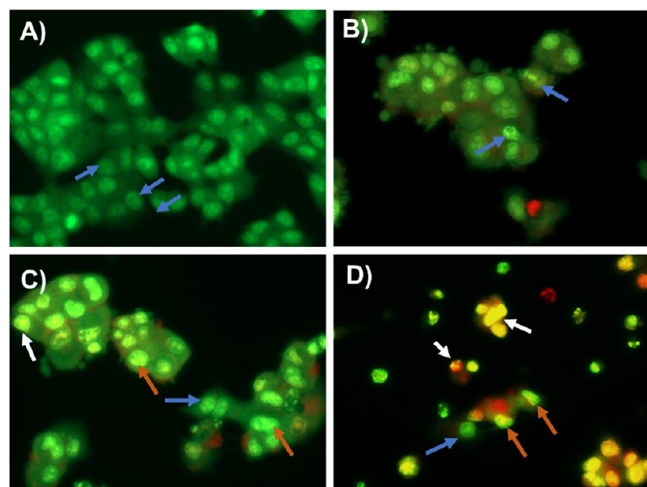
Figure 5. Morphological changes in AO/EtBr-stained MCF-7 cells. (A) Control, (B) PLB, (C) PLB@PLGA-NPs, and (D) RS-PLB@PLGA-NPs treatment. Live cells are indicated by the blue arrow, early apoptotic cells by the brown arrow, and late apoptotic cells by the white arrow.

3.18. ROS Analysis. ROS are highly potent oxidants capable of inducing cell death by increasing intracellular reactive radicals that cause oxidative damage to DNA, proteins, and lipids. PLB blocks the cyclin D3-CDK6 pathway and diminishes the flux of glucose-derived carbon into the pentose phosphate and serine synthesis routes, resulting in a notable elevation of ROS within the tumor.[49] As the concentration of PLB inside the tumor cell increases, ROS production also increases. It was observed from the cellular uptake study that NPs accumulated more in cells compared to free dyes or drugs.

The efficiency of ROS production was investigated in the RS-PLB@PLGA-NPs, PLB@PLGA-NPs, and PLB-treated groups. The level of green fluorescence in the cells was indicative of the level of ROS generated. The levels of fluorescence from phase/green channels were observed for comparison. This is a qualitative analysis for the detection of the level of intracellular ROS. The results demonstrated that RS-PLB@PLGA-NPs exhibit a significantly higher capacity for ROS production compared to PLB@PLGA-NPs and free PLB (Figure 6).
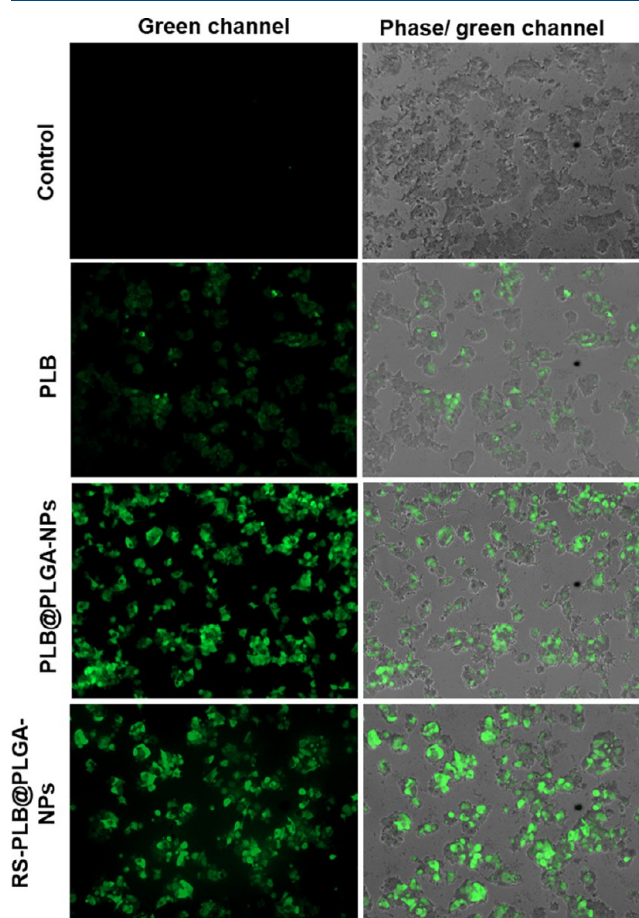
Figure 6. Qualitative intracellular ROS detection by using DCFH-DA following treatment with PLB, PLB@PLGA-NPs, and RS-PLB@PLGA-NPs. The images were captured by a fluorescent microscope.

Control group of cells did not receive any treatment, which was evident from the absence of green fluorescence in the cells. Therefore, based on the obtained data, RS-PLB@PLGA-NPs possess a greater potential for ROS formation in MCF-7 cells compared to PLB@PLGA-NPs and PLB treatments, suggesting their capability to trigger apoptosis more effectively.
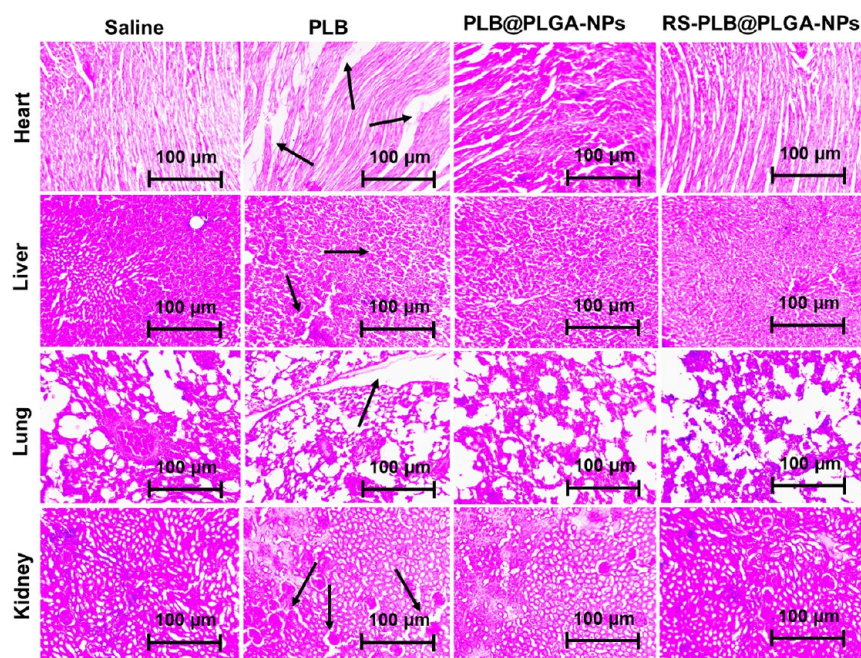
Figure 7. Histopathological investigation of vital organs, including heart, liver, lung, and kidney, after the injection of PLB control, PLB@PLGA-NPs, and RS-PLB@PLGA-NPs. Black arrow shows the location of lesion in the organs.

3.19. Histopathology Study. After 15 days of injection of saline, PLB, PLB@PLGA-NPs, and RS-PLB@PLGA-NPs to rats with a dose of 5.91 mg/kg at 3-day intervals for three times, the histopathologic changes in the heart, liver, lungs, and kidneys were observed by hematoxylin and eosin staining. Figure 7 demonstrates the hematoxylin and eosin-stained vital organs of the rats after treatments with free PLB and developed NPs. Following analysis of the images, it was observed that PLB@PLGA-NPs and RS-PLB@PLGA-NPs treated groups display very less damage to vital organs (heart, liver, lungs, and kidney) compared to the PLB-treated group. Higher damaging nature of the free PLB (indicated by black arrow) was mainly due to the nonspecific distribution to the vital organs. After the entrapment of the PLB into the NPs, limited exposure to the vital organs was the main reason for reduced toxicity.

3.20. In Vivo Antitumor Activity by Photoacoustic and Ultrasound Imaging. The research involved analyzing rats with chemically induced breast tumors using photoacoustic and ultrasonic imaging at four specific time points: initially at day 0 before any treatment and subsequently at days 3, 6, and 10 post initial examination. Figure S5 represents ultrasound imaging of the breast tumor before and after treatment with PLB, PLB@PLGA-NPs, and RS-PLB@PLGA-NPs. The study revealed a significant reduction in the size of the breast tumors following the introduction of redox-sensitive NPs. In contrast, the untreated rats, given only saline, exhibited an increase in the tumor size. However, the group treated with free PLB showed no significant growth in the tumors, indicating a stabilization or static nature in tumor development. Additionally, nonredox-sensitive NPs exhibit slight reduction in the tumor size (Figure S6A).

Tissue hypoxia occurs when cells receive an insufficient supply of oxygen, leading to compromised biological processes. In solid malignant tumors, hypoxia is a common feature due to the inadequate delivery of oxygen within a distance of 70 to 150 μm from the tumor's vascular system.[50] This shortage of oxygen is a result of the rapid proliferation of cancerous cells, creating a scenario where cells are deprived of the necessary oxygen for normal function.[51] Breast cancer treatment is significantly influenced by tumor hypoxia, which is characterized by low oxygen levels, leading to a 3-fold increase in therapeutic resistance compared to tumors with normal oxygen levels. Figure 8A shows the hypoxic tumor region before and after treatment with PLB, PLB@PLGA-NPs, and RS-PLB@PLGA-NPs. PLB indirectly reduced hypoxic tumor by arresting the cell cycle progressing, leading to the slow down of the tumor growth. Thus, a reduction in the tumor growth alleviates the demand for oxygen and nutrients within the tumor microenvironment. As a result, the decreased metabolic load was able to prevent the tumor from becoming hypoxic. The level of PLB within the tumor cells affects the level of hypoxia reduction. Free PLB was less taken by cells and easily effluxed out by cells, whereas PLB@PLGA-NPs and RS-PLB@PLGA-NPs contain TPGS (P-gp efflux pump inhibitor) in the formulation that promoted the accumulation of NPs within the tumor cells. The redox-sensitive NPs were more sensitive toward the tumor microenvironment compared to nonredox-sensitive NPs. This study demonstrated that redox-sensitive NPs were able to treat hypoxic tumor more significantly compared with nonredox-sensitive and free PLB. Further, quantification of the average oxygen saturation (sO_2 %) from the ROI of each breast tumor was performed by Vevo Lab software and graph was plotted (Figure S6B). The obtained data demonstrated that following treatment with the developed formulation, the sO_2 % level was improved more significantly in the RS-PLB@PLGA-NPs-treated group compared to PLB@PLGA-NPs and free PLB.

Tumors require consistent nourishment to grow, which involves stimulating the development of blood vessels around and within the tumor, a process known as angiogenesis.[52,53] In this experiment, the administration of RS-PLB@PLGA-NPs resulted in a noteworthy outcome. Initially, this treatment stopped the process of angiogenesis and then showed a gradual reduction over time. By the 10th day of treatment, a considerable decrease in angiogenesis was observed in the
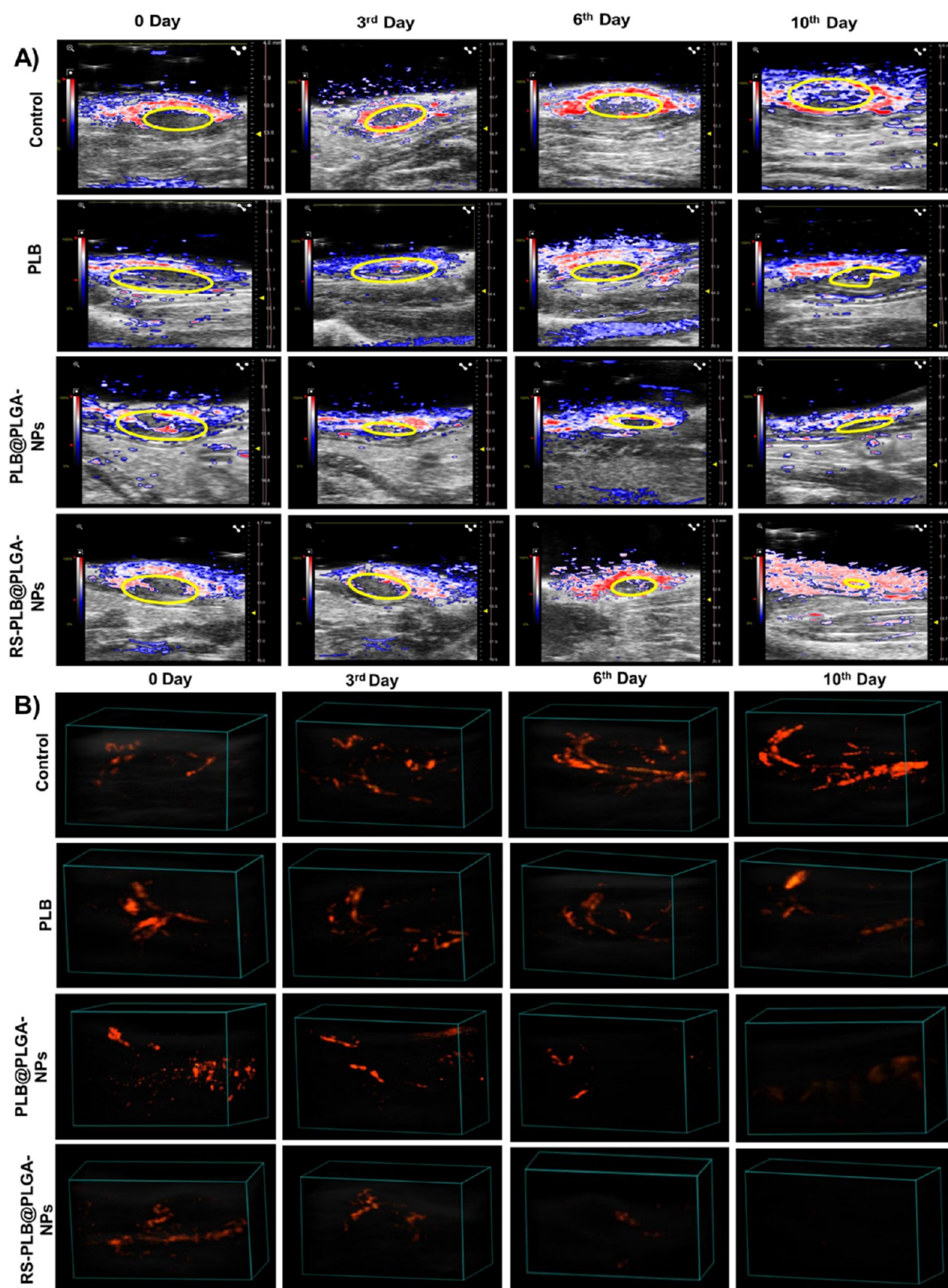
Figure 8. (A) Ultrasound/photoacoustic imaging showing the hypoxic tumor region before and after treatment; yellow circle showing the location of the tumor; scale (red to blue) represents oxygen saturation (sO$_2$) from 100 to 0. (B) Power Doppler imaging of breast tumor showing tumor vascularity.

group receiving RS-PLB@PLGA-NPs, as clearly demonstrated in Figure 8B. Comparatively, the group treated with PLB@

PLGA-NPs displayed a more modest reduction in tumor vasculature by the sixth day. However, by the 10th day, this
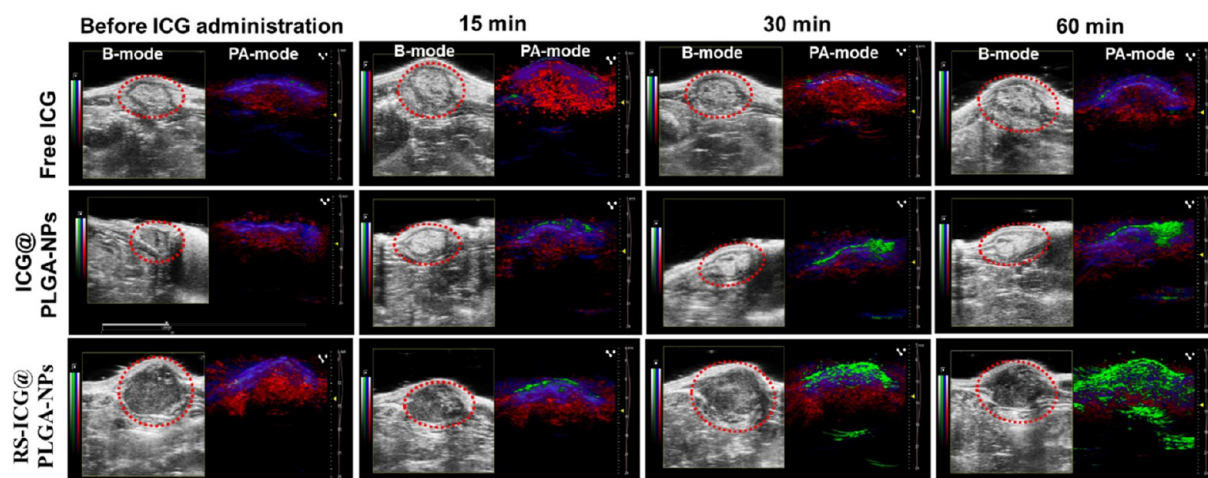
Figure 9. Ultrasound/photoacoustic imaging showing delivery of ICG, ICG@PLGA-NPs, and RS-ICG@PLGA-NPs to the breast tumor; red circle shows the location of the breast tumor. PA images show green signals from ICG, red from oxyhemoglobin, and blue from deoxyhemoglobin.

group also exhibited a significant decrease in tumor angiogenesis. Additionally, an experimental group receiving free PLB treatment showed a slight decrease in tumor angiogenesis. Contrasting these results, the control group of rats displayed a gradual increase in tumor vasculature over the 10-day period (Figure S6C). This experiment highlights the potential of RS-PLB@PLGA-NPs in significantly reducing tumor angiogenesis compared to the other treatments and the natural progression observed in the control group.

3.21. In Vivo Tumor Targeting Efficiency. ICG is a fluorescent dye clinically approved and has an excitation peak at 789 nm and an emission peak at 814 nm. At these excitation and emission wavelengths, there will be no interference from endogenous chromophores. Following the injection of free ICG and ICG-loaded NPs to the rats bearing breast tumor, ultrasound and photoacoustic imaging were performed to observe the distribution of ICG within the breast tumor before and after administration of free ICG and ICG@PLGA-NPs and RS-ICG@PLGA-NPs. Figure 9 depicts the delivery of free ICG and ICG-loaded PLGA-NPs to the breast tumor. In the images, the red circle shows the location of the breast tumor. DMBA-induced breast tumor rat model treated with ICG control, ICG@PLGA-NPs, and RS-ICG@PLGA-NPs showed photoacoustic signal in the breast tumors. The presence of NPs was revealed by green photoacoustic signals within the tumor. After administration of free ICG and formulations, the signals were captured at 15, 30, and 60 min. The study demonstrated that RS-ICG@PLGA-NPs have significantly accumulated in the breast tumor compared to ICG@PLGA-NPs and free ICG. Redox-sensitive NPs had greater affinity toward the tumor microenvironment compared to nonredox-sensitive and free ICG. Additionally, for rats administered with saline, green signals were absent in PA imaging (Figure S7).

4. CONCLUSIONS

In this study, redox-sensitive PLGA-NPs were fabricated by an emulsification-solvent evaporation method for breast cancer imaging and therapy. The synthesis of redox-sensitive polymeric conjugate TPGS-SH was confirmed by FTIR. The PS, PDI, ZP, and EE were found to be in a satisfactory range. The synthesized PLGA-NPs were tested for different physicochemical parameters, including SEM, TEM, XRD, TGA, and DSC. RS-PLB@PLGA-NPs displayed a significant release of drug at a higher GSH concentration and acidic pH in comparison to PLB@PLGA-NPs. XPS survey displayed the characteristic S 2p peak in RS-PLB@PLGA-NPs, indicating that thiol's sulfur is present on the surface of redox-sensitive NPs. In vitro cellular uptake studies revealed the enhanced uptake of RS-C6-CTS-PLGA-NPs compared to free C6 and C6@PLGA-NPs. Both RS-PLB@PLGA-NPs and PLB@PLGA-NPs are stable at 25 and 2−8 °C, as revealed by in vitro stability studies. The IC_{50} values of PLB@PLGA-NPs and RS-PLB@PLGA-NPs toward the breast cancer cell line were 5.24-fold and 14.53-fold higher than free PLB, respectively. Further, ROS and AO/EtBr assay demonstrated superior activity of RS-PLB@PLGA-NPs over PLB@PLGA-NPs and free PLB. Moreover, ultrasound and photoacoustic imaging in the DMBA breast tumor model confirmed significant antitumor activity of the RS-PLB@PLGA-NPs. Further, targeting efficiencies of ICG-loaded NPs were confirmed by ultrasound/photoacoustic imaging. The PLB@PLGA-NPs and RS-PLB@PLGA-NPs were nonhemolytic to human blood. The safety profile of the fabricated PLGA-NPs toward the heart, liver, lungs, and kidney was revealed by in vivo histopathologic studies.

■ ASSOCIATED CONTENT

Ⓢ Supporting Information

The Supporting Information is available free of charge at https://pubs.acs.org/doi/10.1021/acs.molpharmaceut.3c01086.

> FTIR peak assignment of TPGS, TPGS-COOH, and TPGS-SH; DSC curves of TPGS, TPGS-COOH, TPGS-SH, PLGA, PLB@PLGA-NPs, and RS-PLB@PLGA-NPs; TGA curves of TPGS, TPGS-COOH, TPGS-SH, PLGA, PLB@PLGA-NPs, and RS-PLB@PLGA-NPs; effect of storage stability on the PS and PDI; serum storage stability; XPS analysis and atomic percentage of carbon, oxygen, and nitrogen in PLB@PLGA-NPs and RS-PLB@PLGA-NPs; XRD of TPGS, TPGS-COOH, TPGS-SH, PLGA, PLB@PLGA-NPs, and RS-PLB@PLGA-NPs; percentage PLB release at pH 7.4 and pH 5.5; in vivo ultrasound imaging of the rats' breast tumor; graph of % tumor size reduction, % sO_2 saturation and tumor vascularity; and ultrasound/photoacoustic imaging of rats' breast tumor administered with saline (PDF)

■ AUTHOR INFORMATION

Corresponding Authors

Biplob Koch — *Genotoxicology and Cancer Biology Lab, Department of Zoology, Institute of Science, Banaras Hindu University, Varanasi, Uttar Pradesh 221005, India;* orcid.org/0000-0001-9093-7793; Email: biplob@bhu.ac.in

Madaswamy S. Muthu — *Department of Pharmaceutical Engineering and Technology, Indian Institute of Technology (BHU), Varanasi, Uttar Pradesh 221005, India;* orcid.org/0000-0001-5805-7921; Phone: +91 9235195928; Email: msmuthu.phe@itbhu.ac.in; Fax: +91 542 2368428

Authors

Piyush Dhamija — *Department of Pharmaceutical Engineering and Technology, Indian Institute of Technology (BHU), Varanasi, Uttar Pradesh 221005, India*

Abhishesh Kumar Mehata — *Department of Pharmaceutical Engineering and Technology, Indian Institute of Technology (BHU), Varanasi, Uttar Pradesh 221005, India*

Rupen Tamang — *Genotoxicology and Cancer Biology Lab, Department of Zoology, Institute of Science, Banaras Hindu University, Varanasi, Uttar Pradesh 221005, India*

Jyoti Bonlawar — *Department of Pharmaceutical Engineering and Technology, Indian Institute of Technology (BHU), Varanasi, Uttar Pradesh 221005, India*

Vaishali — *Department of Pharmaceutical Engineering and Technology, Indian Institute of Technology (BHU), Varanasi, Uttar Pradesh 221005, India*

Ankit Kumar Malik — *Department of Pharmaceutical Engineering and Technology, Indian Institute of Technology (BHU), Varanasi, Uttar Pradesh 221005, India*

Aseem Setia — *Department of Pharmaceutical Engineering and Technology, Indian Institute of Technology (BHU), Varanasi, Uttar Pradesh 221005, India*

Shailendra Kumar — *SATHI, Central Discovery Centre, Banaras Hindu University, Varanasi, Uttar Pradesh 221005, India*

Ranadheer Reddy Challa — *Department of Pharmaceutical Science, School of Applied Sciences and Humanities, VIGNAN'S Foundation for Science, Technology and Research, Guntur, Andhra Pradesh 522213, India*

Complete contact information is available at:
https://pubs.acs.org/10.1021/acs.molpharmaceut.3c01086

Author Contributions

[⊥]P.D. and A.K.M. contributed equally to this research work.

Notes

The authors declare no competing financial interest.

■ ACKNOWLEDGMENTS

■ REFERENCES

(1) Łukasiewicz, S.; Czeczelewski, M.; Forma, A.; Baj, J.; Sitarz, R.; Stanisławek, A. Breast cancer-epidemiology, risk factors, classification, prognostic markers, and current treatment strategies-an updated review. *Cancers (Basel)* **2021**, *13* (17), 4287.

(2) Sung, H.; Ferlay, J.; Siegel, R. L.; Laversanne, M.; Soerjomataram, I.; Jemal, A.; Bray, F. Global Cancer Statistics 2020: GLOBOCAN estimates of incidence and mortality worldwide for 36 cancers in 185 countries. *CA Cancer J. Clin* **2021**, *71* (3), 209−249.

(3) Mehrotra, R.; Yadav, K. Breast cancer in India: Present scenario and the challenges ahead. *World J. Clin Oncol* **2022**, *13* (3), 209−218.

(4) Harbeck, N.; Penault-Llorca, F.; Cortes, J.; Gnant, M.; Houssami, N.; Poortmans, P.; Ruddy, K.; Tsang, J.; Cardoso, F. Breast cancer. *Nat. Rev. Dis. Primers* **2019**, *5* (1), 66.

(5) Anders, C.; Carey, L. A. Understanding and treating triple-negative breast cancer. *Oncology (Williston Park)* **2008**, *22* (11), 1233−1239. discussion 1239−40, 1243

(6) Puhalla, S.; Bhattacharya, S.; Davidson, N. E. Hormonal therapy in breast cancer: a model disease for the personalization of cancer care. *Mol. Oncol* **2012**, *6* (2), 222−236.

(7) Makadia, H. K.; Siegel, S. J. Poly Lactic-co-Glycolic Acid (PLGA) as biodegradable controlled drug delivery carrier. *Polymers (Basel)* **2011**, *3* (3), 1377−1397.

(8) Lü, J. M.; Wang, X.; Marin-Muller, C.; Wang, H.; Lin, P. H.; Yao, Q.; Chen, C. Current advances in research and clinical applications of PLGA-based nanotechnology. *Expert Rev. Mol. Diagn* **2009**, *9* (4), 325−341.

(9) El-Hammadi, M. M.; Arias, J. L. Recent advances in the surface functionalization of PLGA-based nanomedicines. *Nanomaterials (Basel)* **2022**, *12* (3), 354 DOI: 10.3390/nano12030354.

(10) Dodda, J. M.; Remiš, T.; Rotimi, S.; Yeh, Y. C. Progress in the drug encapsulation of poly (lactic-co-glycolic acid) and folate-decorated poly (ethylene glycol)-poly (lactic-co-glycolic acid) conjugates for selective cancer treatment. *J. Mater. Chem. B* **2022**, *10* (22), 4127−4141.

(11) Lu, B.; Lv, X.; Le, Y. Chitosan-modified PLGA nanoparticles for control-released drug delivery. *Polymers (Basel)* **2019**, *11* (2), 304.

(12) Rathod, S.; Bahadur, P.; Tiwari, S. Nanocarriers based on vitamin E-TPGS: Design principle and molecular insights into improving the efficacy of anticancer drugs. *Int. J. Pharm.* **2021**, *592*, No. 120045.

(13) Yan, A.; Von Dem Bussche, A.; Kane, A. B.; Hurt, R. H. Tocopheryl polyethylene glycol succinate as a safe, antioxidant surfactant for processing carbon nanotubes and fullerenes. *Carbon N Y* **2007**, *45* (13), 2463−2470.

(14) Zhang, Z.; Tan, S.; Feng, S. S. Vitamin E TPGS as a molecular biomaterial for drug delivery. *Biomaterials* **2012**, *33* (19), 4889−4906.

(15) Muthu, M. S.; Mei, L.; Feng, S. S. Nanotheranostics: advanced nanomedicine for the integration of diagnosis and therapy. *Nanomedicine (Lond)* **2014**, *9* (9), 1277−1280.

(16) Viswanadh, M. K.; Agrawal, N.; Azad, S.; Jha, A.; Poddar, S.; Mahto, S. K.; Muthu, M. S. Novel redox-sensitive thiolated TPGS based nanoparticles for EGFR targeted lung cancer therapy. *Int. J. Pharm.* **2021**, *602*, No. 120652.

(17) Piezzo, M.; Cocco, S.; Caputo, R.; Cianniello, D.; Gioia, G. D.; Lauro, V. D.; Fusco, G.; Martinelli, C.; Nuzzo, F.; Pensabene, M.; De Laurentiis, M. Targeting cell cycle in breast cancer: CDK4/6 inhibitors. *Int. J. Mol. Sci.* **2020**, *21* (18), 6479 DOI: 10.3390/ijms21186479.

(18) Braal, C. L.; Jongbloed, E. M.; Wilting, S. M.; Mathijssen, R. H. J.; Koolen, S. L. W.; Jager, A. Inhibiting CDK4/6 in Breast cancer with palbociclib, ribociclib, and abemaciclib: similarities and differences. *Drugs* **2021**, *81* (3), 317−331.

(19) Parsian, M.; Mutlu, P.; Taghavi Pourianazar, N.; Yalcin Azarkan, S.; Gunduz, U. Investigation of the therapeutic effects of palbociclib conjugated magnetic nanoparticles on different types of breast cancer cell lines. *Cell. Mol. Bioeng.* **2023**, *16*, 143−157.

(20) Lian, H.; He, Z.; Meng, Z. Rational design of hybrid nanomicelles integrating mucosal penetration and P-glycoprotein inhibition for efficient oral delivery of paclitaxel. *Colloids Surf. B Biointerfaces* **2017**, *155*, 429−439.

(21) Setia, A.; Kumari, P.; Vikas; Kumar Mehata, A.; Kumar Malik, A.; Kumar Mahto, S.; Muthu, M. S. Cetuximab decorated redox sensitive D-alpha-tocopheryl- polyethyleneglycol-1000-succinate based nanoparticles for cabazitaxel delivery: Formulation, lung targeting and enhanced anti-cancer effects. *Int. J. Pharm.* **2024**, *653*, No. 123881.

(22) Mazzarella, L.; Guida, A.; Curigliano, G. Cetuximab for treating non-small cell lung cancer. *Expert Opin Biol. Ther* **2018**, *18* (4), 483–493.

(23) Kızılbey, K. Optimization of rutin-loaded PLGA nanoparticles synthesized by single-emulsion solvent evaporation method. *Acs Omega* **2019**, *4* (1), 555–562.

(24) Cavalu, S.; Prokisch, J.; Laslo, V.; Vicas, S. Preparation, structural characterisation and release study of novel hybrid microspheres entrapping nanoselenium, produced by green synthesis. *IET Nanobiotechnol* **2017**, *11* (4), 426–432.

(25) Chourasiya, V.; Bohrey, S.; Pandey, A. Formulation, optimization, and characterization of amlodipine besylate loaded polymeric nanoparticles. *Polym. Polym. Compos.* **2021**, *29* (9_suppl), S1555–S1568. DOI: 10.1177/09673911211056154.

(26) Xu, K.; Yao, H.; Fan, D.; Zhou, L.; Wei, S. Hyaluronic acid thiol modified injectable hydrogel: Synthesis, characterization, drug release, cellular drug uptake and anticancer activity. *Carbohydr. Polym.* **2021**, *254*, No. 117286.

(27) Alshamsan, A.; Binkhathlan, Z.; Kalam, M. A.; Qamar, W.; Kfouri, H.; Alghonaim, M.; Lavasanifar, A. Mitigation of tacrolimus-associated nephrotoxicity by PLGA Nanoparticulate delivery following multiple dosing to mice while maintaining its immunosuppressive activity. *Sci. Rep.* **2020**, *10* (1), 6675.

(28) Devasvaran, K.; Jairaman, S.; Yahaya, N. A.; Jaganath, I. B. S.; Khung, Y. L.; Lim, V.; Ngalim, S. H. PEG-b-PLGA nanoparticles loaded with Geraniin from Phyllanthus watsonii extract as a phytochemical delivery model. *Appl. Sci.* **2020**, *10* (14), 4891 DOI: 10.3390/app10144891.

(29) Yen, H. J.; Young, Y. A.; Tsai, T. N.; Cheng, K. M.; Chen, X. A.; Chen, Y. C.; Chen, C. C.; Young, J. J.; Hong, P. D. Positively charged gold nanoparticles capped with folate quaternary chitosan: Synthesis, cytotoxicity, and uptake by cancer cells. *Carbohydr. Polym.* **2018**, *183*, 140–150.

(30) Wang, Y.; Wang, S.; Li, C.; Qian, M.; Bu, J.; Wang, J.; Huang, R. Facile growth of well-dispersed and ultra-small MoS2 nanodots in ordered mesoporous silica nanoparticles. *Chem. Commun. (Camb)* **2016**, *52* (67), 10217–10220.

(31) Mehata, A. K.; Singh, V.; Vikas; Srivastava, P.; Koch, B.; Kumar, M.; Muthu, M. S. Chitosan nanoplatform for the co-delivery of palbociclib and ultra-small magnesium nanoclusters: dual receptor targeting, therapy and imaging. *Nanotheranostics* **2024**, *8* (2), 179–201.

(32) Hakeem, A.; Zahid, F.; Zhan, G.; Yi, P.; Yang, H.; Gan, L.; Yang, X. Polyaspartic acid-anchored mesoporous silica nanoparticles for pH-responsive doxorubicin release. *Int. J. Nanomedicine* **2018**, *13*, 1029–1040.

(33) Abdelwahab, T. S.; Abdelhamed, R. E.; Ali, E. N.; Mansour, N. A.; Abdalla, M. S. Evaluation of silver nanoparticles caffeic acid complex compound as new potential therapeutic agent against cancer incidence in mice. *Asian Pac J. Cancer Prev* **2021**, *22* (10), 3189–3201.

(34) Garms, B. C.; Poli, H.; Baggley, D.; Han, F. Y.; Whittaker, A. K.; Anitha, A.; Grøndahl, L. Evaluating the effect of synthesis, isolation, and characterisation variables on reported particle size and dispersity of drug loaded PLGA nanoparticles. *Mater. Adv.* **2021**, *2* (17), 5657–5671.

(35) Mehata, A. K.; Singh, V.; Vikas; Singh, N.; Mandal, A.; Dash, D.; Koch, B.; Muthu, M. S. Chitosan-g-estrone nanoparticles of palbociclib vanished hypoxic breast tumor after targeted delivery: development and ultrasound/photoacoustic imaging. *ACS Appl. Mater. Interfaces* **2023**, *15* (29), 34343–34359.

(36) Xue, P.; Liu, D.; Wang, J.; Zhang, N.; Zhou, J.; Li, L.; Guo, W.; Sun, M.; Han, X.; Wang, Y. Redox-Sensitive citronellol-cabazitaxel conjugate: maintained in vitro cytotoxicity and self-assembled as multifunctional nanomedicine. *Bioconjug Chem.* **2016**, *27* (5), 1360–1372.

(37) Al-Baker, A.; Al-Kshab, A.; Ismail, H. K.; Ashwaq, A. Effect of silver nanoparticles on some blood parameters in rats. *Iraqi J. Vet Sci.* **2020**, *34* (2), 389–395.

(38) Wu, H.; Su, M.; Jin, H.; Li, X.; Wang, P.; Chen, J.; Chen, J. Rutin-Loaded Silver Nanoparticles With Antithrombotic Function. *Front Bioeng Biotechnol* **2020**, *8*, No. 598977.

(39) Ramadass, S. K.; Anantharaman, N. V.; Subramanian, S.; Sivasubramanian, S.; Madhan, B. Paclitaxel/epigallocatechin gallate coloaded liposome: a synergistic delivery to control the invasiveness of MDA-MB-231 breast cancer cells. *Colloids Surf. B Biointerfaces* **2015**, *125*, 65–72.

(40) Ye, J.; Xia, X.; Dong, W.; Hao, H.; Meng, L.; Yang, Y.; Wang, R.; Lyu, Y.; Liu, Y. Cellular uptake mechanism and comparative evaluation of antineoplastic effects of paclitaxel-cholesterol lipid emulsion on triple-negative and non-triple-negative breast cancer cell lines. *Int. J. Nanomedicine* **2016**, *11*, 4125–4140.

(41) Govindaraju, S.; Roshini, A.; Lee, M. H.; Yun, K. Kaempferol conjugated gold nanoclusters enabled efficient for anticancer therapeutics to A549 lung cancer cells. *Int. J. Nanomedicine* **2019**, *14*, 5147–5157.

(42) Jabir, M. S.; Nayef, U. M.; Abdulkadhim, W. K.; Taqi, Z. J.; Sulaiman, G. M.; Sahib, U. I.; Al-Shammari, A. M.; Wu, Y.-J.; El-Shazly, M.; Su, C.-C. Fe 3 O 4 nanoparticles capped with PEG induce apoptosis in breast cancer AMJ13 cells via mitochondrial damage and reduction of NF-κB translocation. *J. Inorg. Organomet. Polym. Mater.* **2021**, *31*, 1241–1259.

(43) Kim, H.; Xue, X. Detection of total reactive oxygen species in adherent cells by 2′,7′-dichlorodihydrofluorescein diacetate staining. *J. Vis. Exp.* **2020**, *160*, No. e60682, DOI: 10.3791/60682.

(44) Lari, A. S.; Zahedi, P.; Ghourchian, H.; Khatibi, A. Microfluidic-based synthesized carboxymethyl chitosan nanoparticles containing metformin for diabetes therapy: In vitro and in vivo assessments. *Carbohydr. Polym.* **2021**, *261*, No. 117889.

(45) Raes, F.; Sobilo, J.; Le Mée, M.; Rétif, S.; Natkunarajah, S.; Lerondel, S.; Le Pape, A. High resolution ultrasound and photoacoustic imaging of orthotopic lung cancer in mice: new perspectives for onco-pharmacology. *PLoS One* **2016**, *11* (4), No. e0153532.

(46) Seshadri, V. D.; Oyouni, A. A. A.; Bawazir, W. M.; Alsagaby, S. A.; Alsharif, K. F.; Albrakati, A.; Al-Amer, O. M. Zingiberene exerts chemopreventive activity against 7, 12-dimethylbenz (a)anthracene-induced breast cancer in Sprague-Dawley rats. *J. Biochem. Mol. Toxicol.* **2022**, *36* (10), No. e23146.

(47) Xu, X.; Wu, H.; Yang, Y.; Liu, B.; Tian, J.; Bao, H.; Liu, T. PLGA-coated methylene blue nanoparticles for photoacoustic imaging and photodynamic/photothermal cascaded precisely synergistic therapy of tumor. *RSC Adv.* **2022**, *12* (3), 1543–1549.

(48) Vikas; Mehata, A. K.; Viswanadh, M. K.; Malik, A. K.; Setia, A.; Kumari, P.; Mahto, S. K.; Muthu, M. S. EGFR targeted redox sensitive chitosan nanoparticles of cabazitaxel: dual-targeted cancer therapy, lung distribution, and targeting studies by photoacoustic and optical imaging. *Biomacromolecules* **2023**, *24* (11), 4989–5003.

(49) Huang, Z.; Hu, H.; Xian, T.; Xu, Z.; Tang, D.; Wang, B.; Zhang, Y. Carrier-free nanomedicines self-assembled from palbociclib dimers and Ce6 for enhanced combined chemo-photodynamic therapy of breast cancer. *RSC Adv.* **2023**, *13* (3), 1617–1626.

(50) Li, Y.; Zhao, L.; Li, X. F. Hypoxia and the tumor microenvironment. *Technol. Cancer Res. Treat.* **2021**, *20*, No. 15330338211036304.

(51) Coates, J. T.; Skwarski, M.; Higgins, G. S. Targeting tumour hypoxia: shifting focus from oxygen supply to demand. *Br. J. Radiol.* **2019**, *92* (1093), No. 20170843.

(52) Claesson-Welsh, L.; Welsh, M. VEGFA and tumour angiogenesis. *J. Intern Med.* **2013**, *273* (2), 114–127.

(53) De Palma, M.; Biziato, D.; Petrova, T. V. Microenvironmental regulation of tumour angiogenesis. *Nat. Rev. Cancer* **2017**, *17* (8), 457–474.